Journal of Molecular Catalysis A: Chemical 353–354 (2012) 95–105

Contents lists available at SciVerse ScienceDirect

Journal of Molecular Catalysis A: Chemical

journal homepage: www.elsevier.com/locate/molcata

Sulfated fibrous ZrO_2/Al_2O_3 core and shell nanocomposites: A novel strong acid catalyst with hierarchically macro–mesoporous nanostructure

Erming Liu, Ashley J. Locke, Ray L. Frost*, Wayde N. Martens

Discipline of Chemistry, Faculty of Science and Technology, Queensland University of Technology, GPO Box 2434, Brisbane, Queensland 4001, Australia

ARTICLE INFO

Article history:
Received 21 September 2011
Received in revised form 6 November 2011
Accepted 7 November 2011
Available online 17 November 2011

Keywords:
Sulfated ZrO_2/Al_2O_3
Fibrous catalyst
Core–shell nanocomposite
Hierarchical nanostructure
Benzoylation of toluene

ABSTRACT

A series of solid strong acid catalysts were synthesized from fibrous ZrO_2/Al_2O_3 core and shell nanocomposites. In this series, the zirconium molar percentage was varied from 2% to 50%. The ZrO_2/Al_2O_3 nanocomposites and their solid strong acid counterparts were characterised by a variety of techniques including ^{27}Al magic angle spinning nuclear magnetic resonance (MAS-NMR), scanned electronic microscopy (SEM), transmission electron microscope (TEM), X-ray photoelectron spectroscopy (XPS), nitrogen adsorption and infrared emission spectroscopy (IES). NMR results show that the interaction between zirconia species and alumina strongly correlates with pentacoordinated aluminium sites. This can also be detected by the change in binding energy of the 3d electrons of the zirconium.

The acidity of the obtained solid acids was tested by using them as catalysts for the benzoylation of toluene. It was found that a sample with a 50% zirconium molar percentage possessed the highest surface acidity equalling that of pristine sulfated zirconia despite the reduced mass of zirconia.

1. Introduction

Sulfated zirconia was first prepared and explored as a hydrocarbon isomerisation catalyst by Holm and Bailey [1] in 1962. Its unique acid catalytic activity was reported in the literature by Hino et al. in 1979, that this catalyst can transform butane into isobutane even at room temperature [2]. Since then, numerous studies using sulfated zirconia as an acid catalyst appeared [3,4]. It represents a new class of solid strong acid catalysts, and can carry out reactions involving very strong acid sites under mild temperature conditions [5,6]. Moreover, it possesses distinct advantages in catalyst separation, reactive-system maintenance, compared with traditional liquid catalyst, such as HF and H_2SO_4, which cannot satisfy the stringent environmental restriction on waste disposal [7,8].

Several zirconium precursors have been reported for the preparation of sulfated zirconia, usually, the catalyst is prepared by first precipitating the hydroxide of zirconium which, after washing and drying, subsequently is treated with a solution of H_2SO_4 and followed by calcination. In the preparation procedures, the pH of precipitation of the hydroxide step [9], and the calcination temperature [10,11] are found to be particularly important for a high catalytic activity. The optimised calcination temperature is found at 600–650 °C to give the highest intrinsic activity [10] corresponding to the formation of theoretical monolayer coverage by the sulfated species. Moreover, the treatment with other sulfurous species, such as $(NH_4)_2SO_4$, SO_2, H_2S, and SO_3 can also promote its catalytic activity [12]. Morterra et al. [13] investigated the relationship between the crystal phase of zirconia and their exhibited catalytic activity, and proposed that (i) the sulfation process usually occurs irrespective of sulfating agent; (ii) the zirconia must be tetragonal phase in the final catalyst while the catalyst as monoclinic zirconia is almost inactive as investigated in the isomerisation reaction of n-alkanes; (iii) the catalyst must be activated by calcination at temperatures $T \geq 800$ K, at this temperature, the surface sulfates on tetragonal zirconia are corresponding to a structure, in which the two S=O oscillators almost form an orthogonal angle.

Pristine sulfated zirconia appears as a very promising solid acid catalyst for the replacement of the commercial acid catalyst; however, the catalyst is known to suffer significant deactivation in practical application, possibly due to sulfur leaching or reduction at mild temperatures, active phase transformation from tetragonal phase to monoclinic phase, or the formation of coke on the surface of catalyst [14].

Mounting the sulfate zirconia on an alumina support [11] was proposed to constitute a more stable catalyst capable of resisting deactivation. However, it is hard to attain a high loading of zirconium species on this support because the particle aggregation and sintering during preparations can sufficiently decrease the specific surface area, resulting in negative effect on catalytic activity [15]. Unfortunately, a small loading of zirconia cannot give rise to the highly active tetragonal zirconia [11,16].

* Corresponding author. Tel.: +61 731382407; fax: +61 731381804.
E-mail address: r.frost@qut.edu.au (R.L. Frost).

1381-1169/$ – see front matter © 2011 Elsevier B.V. All rights reserved.
doi:10.1016/j.molcata.2011.11.010

Gao reported [17,18] that sulfated zirconia promoted by a small amount of alumina by co-precipitation exhibited excellent catalytic activity and also improved stability at the temperature higher than 250 °C for n-butane isomerization. The roles of alumina were investigated by several groups [18–20]. The increase in activity for n-butane isomerisation was attributed to a significant increase in the concentration of active sites. Addition of Al_2O_3 also results in the formation of smaller crystallites of ZrO_2 which stabilise the active tetragonal phase of ZrO_2. The presence of smaller crystallite sizes of the tetragonal phase of ZrO_2 after Al_2O_3-promotion affects the total surface area, sulfur content and the number of active sites.

However, the samples prepared by co-precipitation or sol–gel method have an inherent limitation. During the preparation of ZrO_2/Al_2O_3 nanocomposite, as a result of the homogeneous distribution of Zr and Al at atomic level, the addition of only a small fraction of aluminium by these methods will result in a significant elevation of calcination temperature for the phase transformation from the resultant amorphous precipitate to tetragonal ZrO_2 nanocrystallites. For example, as reported in Gao's papers [17,18], the addition of 15 mol% Al_2O_3 in the synthesis of Al_2O_3-promoted sulfated zirconia resulted in an amorphous material after calcination at 650 °C. The crystallizing temperature of this material had to be elevated to 750 °C to achieve tetragonal structure of zirconia, given the relatively low activity of the amorphous zirconia solid acid [21]. Nevertheless, such high calcination temperature not only decomposed sulfate species, but also resulted in low surface areas of this material [18]. Moreover, the increase of calcination temperature in such a high temperature region will bring about not only extremely large amount of energy waste but also expensive investment for thermal insulation on an industrial scale.

In our previous investigation [22], tetragonal zirconia nanocrystallites were supported on long bundles of alumina nanofibres forming extremely long ZrO_2/Al_2O_3 composite nanorods with a new core–shell structure when the Zr molar percentage was >30%. Naturally, the resultant materials are a hierarchically macro–mesoporous zirconia material: the evenly distributed ZrO_2 nanocrystallites result in mesoporous zirconia with large surface areas, while the stacking of such nanorods gives rise to a new kind of macroporous material. The stabilised and highly dispersed tetragonal zirconia nanocrystallites observed on fibrous ZrO_2/Al_2O_3 core–shell nanocomposites and the unique property of tetragonal zirconia on catalytic application provide intense incentive to us to develop these nanocomposites into a series of novel catalysts. In this work, these fibrous ZrO_2/Al_2O_3 core–shell nanocomposites were developed as a series of fibrous solid acid with the Zr molar percentage $X = 100 \times Zr/(Al + Zr)$ from 2% to 50% via sulfating procedure, followed by calcining at 650 °C.

Benzoylation of toluene with benzoyl chloride is an important strong acid-catalysed reaction for the manufacture of aromatic ketones, which are important intermediates in the fine-chemical and pharmaceutical industries. The catalytic performances of many other solid acids, including zeolite [23], Nafion-H on silica [24], heteropolyacids [25] and some sulfated metal oxide [26] such as SO_4^{2-}/γ-Al_2O_3, SO_4^{2-}/ZrO_2 have been evaluated for this reaction to replace some homogeneous acid catalysts used in industry. On sulfated zirconia, the product of the benzoylation of toluene with benzoyl chloride is a mixture of *p*-, *o*- and *m*-methylbenzophenone (Scheme 1). The catalytic performances of fibrous sulfated nanocomposites were tested for this reaction. The structure and physicochemical properties of the catalysts were characterised by means of XRD, IES, SEM equipped with EDX, ^{27}Al MAS NMR and the N_2 adsorption/desorption isotherms.

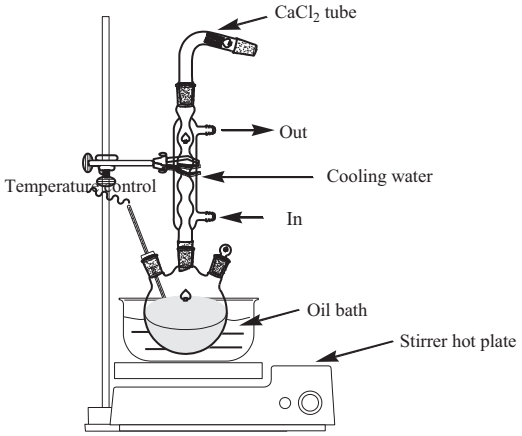

Scheme 1. Benzoylation of toluene with benzoyl chloride.

2. Experimental

2.1. Materials

Boehmite fibres were synthesized by steam-assisted, solid wet-gel method according to literature reports [27]. Butanol was purchased from Ajax Finechem and zirconium (IV) tert-butoxide solution (80 wt% in 1-butanol) was purchased from Aldrich. All these chemicals are used as received.

2.2. Nanocomposite preparation

Fibrous $Zr(OH)_x$-boehmite nanocomposites were synthesized by deposition of zirconia species on the boehmite nanofibres. In a typical procedure, 0.39 g boehmite nanofibres was added with 0.20 g deioned water which was then dispersed into 20 ml butanol under vigorous stirring. Zirconium (IV) butoxide was dissolved into the resultant mixture solution according to the Zr molar percentage $X = 100 \times Zr/(Al + Zr) = 2\%, 5\%, 10\%, 15\%, 30\%$, with stirring for 5 min. The nanocomposite with 50% of Zr molar percentage was synthesized by the same procedure as mentioned above, except that 0.39 g boehmite nanofibres was added with 0.40 g deioned water, as the hydrolysis of additional zirconium butoxide consumes more water. Subsequently, the solutions were transferred into autoclaves for hydrothermal reaction at 170 °C for 24 h. After cooling to room temperature, the resulting nanocomposites were separated by centrifugation, and then dried at 80 °C for 1 day.

2.3. Catalyst preparation

To prepare fibrous sulfated nanocomposites, as-synthesized fibrous $Zr(OH)_x$-boehmite nanocomposites with various Zr molar percentage were precalcined at 300 °C for 3 h and re-dispersed into a 0.5 M H_2SO_4 solution (15 ml g^{-1}). After 30 min, the samples were separated by centrifugation and dried at 80 °C for 24 h, followed by calcination at 650 °C in air for 3 h. These sulfated fibrous nanocomposites are labelled as S–Zr-"*m*", where *m* is Zr molar percentage.

For comparison, sulfated zirconia, sulfated alumina and two kinds of commercial zeolites (H-ZSM-5, HY) were chosen as reference catalysts. Sulfated zirconia was prepared according to the procedures in the literatures [17,28]: amorphous $Zr(OH)_4$ was prepared by dropwise addition of aqueous ammonia into a zirconyl solution until pH 9. After washing and drying, the sample was immersed in a 0.5 M H_2SO_4 solution for 30 min followed by separation from the liquid phase. Without washing, the sulfated zirconia was dried at 80 °C and calcined at 650 °C in air for 3 h. The resulting catalyst was labelled as SZ. Sulfated alumina was prepared by

immersing boehmite nanofibres into a 0.5 M H_2SO_4 solution for 30 min followed by separation from the liquid phase. The sample was dried at 80 °C for 24 h, calcined at 650 °C for 3 h and labelled as SA-F.

ZSM-5 was purchased from Zeolyst international (CBV 2314), USA, and zeolite Y was supplied by FuSheng dyestuff factory, China. All the zeolites were received in the ammonium form, and were transformed into corresponding H-zeolites by calcination at 550 °C for 6 h. The surface area of commercial H-ZSM-5 was 425 $m^2\ g^{-1}$ and its reported Si/Al ratio was 11.5. The surface area of commercial HY was 648 $m^2\ g^{-1}$ and its reported Si/Al ratio was 3.

2.4. Characterisation

Sulfate contents of all samples were determined by ion chromatography. The instrument is a Dionex RFIC 2100 ion chromatograph with a Dionex AS-18 4 mm × 100 mm analytical column and an AS18 4 mm × 25 mm guard column. An isocratic 33 mmol KOH solution was used as eluent. All sulfated powdered sample was suspended in 0.1 M NaOH and filtered through a 0.5-μm PTFE filter.

XRD patterns were collected on a PANalytical X'Pert PRO X-ray diffractometer (radius: 240.0 mm). Incident X-ray radiation was produced from a line-focused PW3373/10 Cu X-ray tube, operating at 40 kV and 40 mA, providing a $K\alpha_1$ wavelength of 1.540596 Å. The incident beam passed through a 0.04 rad Soller slit, a 1/2 divergence slit, a 15 mm fixed mask, and a 1° fixed antiscatter slit. After interaction with the sample, the diffracted beam was detected by an X'Celerator RTMS detector, which was set in scanning mode, with an active length of 2.022 mm. Diffraction patterns for the samples were collected over a range of 3–75° 2θ.

XPS data was obtained on a Kratos Axis ULTRA X-ray photoelectron spectrometer. The incident radiation was monochromatic Al X-rays (1486.6 eV) at 150 W (15 kV, 15 mA). The C 1s peak at 284.5 eV was used as a reference for the calibration of binding energy scale. XPS spectra collected was analysed using commercial software (CasaXPS N. Farley, version 2.3.12, 1999–2006).

Surface area analysis based on N_2 adsorption/desorption techniques were performed on a Micrometrics Tristar 3000 automated gas adsorption analyser. Samples were pretreated at 200 °C under the flow of N_2 for a minimum of 5 h on a Micrometrics Flowprep 060 degasser.

SEM micrographs were obtained on a FEI QUANTA 200 scanning electron microscope operating at 30 kV accelerating voltage with a 2.5 spot size. The samples were dried at room temperature and coated with gold under vacuum conditions in an argon atmosphere ionization chamber to increase surface conductivity.

FT-IR emission spectroscopy was carried out on a Nicolet spectrometer modified by replacing the IR source with an emission cell. The description of the cell and principles of the emission experiment have been published elsewhere [29].

Solid-state ^{27}Al MAS NMR spectra were obtained from Varian Driver spectrometer operating at a resonance frequency of 104.26 Hz with a recycling time of 0.5 s. The spinning frequency was no lower than 7 kHz.

Transmission electron microscopy was carried out on a Phillips Tecnai F20 TEM. The instrument was equipped with a Field Emission Gun source operating at a High Tension of 200 kV.

2.5. Benzoylation reaction

Benzoylation of toluene with benzoyl chloride was used to investigate the catalytic activity of a series of fibrous nanocomposite superacids. The reaction was carried out in a round-bottom flask equipped with a reflux condenser connecting with a $CaCl_2$ tube which is used to keep the reaction system free of moisture

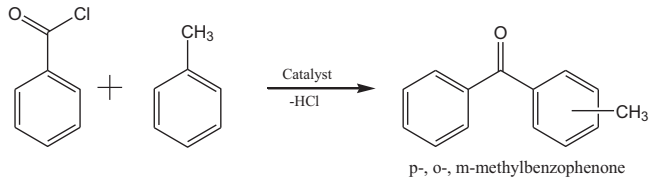

Scheme 2. Schematic diagram of catalytic reactor for benzoylation of toluene with benzoyl chloride.

(Scheme 2). Before reaction, all catalysts were freshly activated at 500 °C for 2.5 h and cooled down to ambient temperature in an argon atmosphere in order to remove the adsorbed water molecules on the surfaces of the catalysts. 0.4 ml benzoyl chloride, 8 ml toluene and 0.2 g catalysts were charged into the reactor which was heated to reflux (*ca.* 110 °C) in an oil bath under magnetic stir. Samples were collected at some specific intervals and immediately analysed by gas chromatography. Quantitative results were obtained by comparing the results with the calibration from synthetic mixtures. Since toluene was in excess, the yields of methylbenzophenone were based on the benzoyl chloride added into the reaction.

3. Results

The overall compositions of all the fibrous nanocomposites prepared with various Zr/Al molar ratios were examined by EDX equipped on SEM. The area selected was approximately 0.04 mm^2 at each run, and at least five different spots were selected for each sample to get an average value of the composition. As shown in Fig. 1, the observed Zr percentage is equal to the nominal molar ratio, indicating all of zirconium precursors were precipitated from the mixture solution and deposited on the boehmite nanofibres.

The XRD patterns of the sulfated fibrous ZrO_2/Al_2O_3 nanocomposites obtained by calcination at 650 °C for 3 h are shown in Fig. 2. The phase of sulfated alumina nanofibres illustrates the γ-Al_2O_3 structure. The peaks at 45.8° and 66.8° 2θ correspond to the diffractions from (4 0 0) and (4 4 0) planes of γ-Al_2O_3. For pristine sulfated zirconia, a small portion of the monoclinic phase presents besides the tetragonal phase. The peaks at 30.2°, 35.3°, 50.3° and 60.1° 2θ are attributed to the diffractions from (1 0 1), (1 1 0), (1 1 2) and (2 1 1) planes of tetragonal zirconia while the peaks at 24.5°, 28.2° 2θ are the diffractions from (−1 1 0) and (−1 1 1) planes of monoclinic zirconia. In contrast, for these sulfated fibrous nanocomposites, as Zr molar percentage is higher than 10%, the nanocrystallites of tetragonal zirconia can be detected

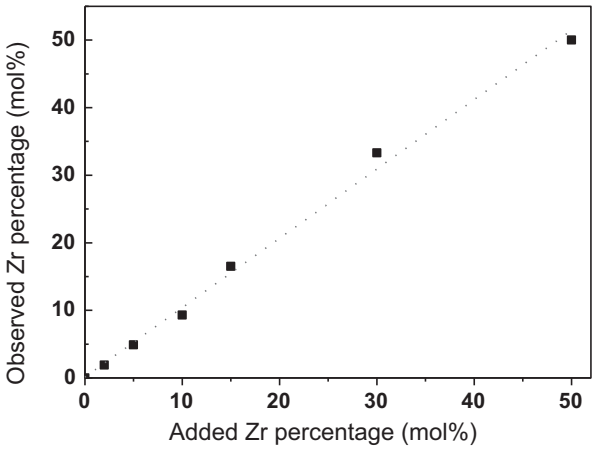

Fig. 1. Observed Zr percentage in samples as a function of nominal Zr percentage (measured by EDX).

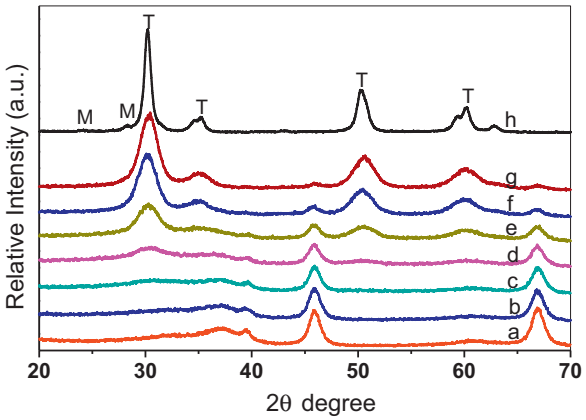

Fig. 2. XRD patterns for the sulfated fibrous ZrO_2/Al_2O_3 nanocomposites, alumina nanofibres and zirconia obtained by calcination at 650 °C for 3 h. (a) Sulfated alumina nanofibres, (b) S–Zr-2, (c) S–Zr-5, (d) S–Zr-10, (e) S–Zr-15, (f) S–Zr-30, (g) S–Zr-50 and (h) sulfated zirconia. M and T represent monoclinic phase and tetragonal phase, respectively. The patterns in (h) underwent a 0.6-fold *Y*-scale reduction.

by the appearance of a broadened peak at *ca.* 30°. The intensity of this diffraction, as well as others for tetragonal zirconia, increases with the increase of zirconia percentage, but no peak corresponding to monoclinic zirconia is observed in the patterns for all these nanocomposites. Meanwhile, the diffraction peaks for γ-Al_2O_3 gradually decrease and become undetectable at 50 mol% of Zr due to the reduction of relative concentration of the γ-Al_2O_3 and its inherently poor intensity.

Table 1
Crystallite dimension in (1 0 1) direction for sulfated tetragonal zirconium and that deposited on alumina nanofibres with various zirconia content (the data were derived from X-ray diffraction patterns).

Sample name	Peak position (2θ)	FWHM (2θ)	Crystallite dimensions (nm)
Sulfated zirconium	30.14	0.684	12.0
S–Zr-50	30.28	1.832	4.5
S–Zr-30	30.12	2.086	3.9
S–Zr-15	30.34	3.057	2.7
S–Zr-10	30.38	4.000	2.1

The primary crystallite sizes of the tetragonal zirconia in these samples (including the pristine sulfated zirconium and fibrous sulfated ZrO_2/Al_2O_3 nanocomposites) are calculated by the Scherrer equation and listed in Table 1. It can be observed that an increase of Zr molar percentage from 10% to 50% resulted in increased main crystallite sizes from 2.1 nm to 4.5 nm in (1 0 1) direction, which are much smaller than that of the pristine sulfated zirconium at 12 nm. As shown in our previous investigation [22], the alumina nanofibres can retard the crystallite size growth of zirconia and therefore retard the transformation of zirconia from metastable tetragonal phase to the monoclinic phase because metastable tetragonal zirconia is stable in small crystal size.

Fig. 3 shows the ^{27}Al MAS NMR spectra of the sulfated fibrous nanocomposites. Although it is possible that some spectral components cannot be distinguished due to peak broadening, some species can be clearly identified via fitting procedures, as shown in Fig. 4. The intense signal at *ca.* 5 ppm corresponds to octahedral aluminium Al_{octa} sites (AlO_6), while the relatively weak resonances

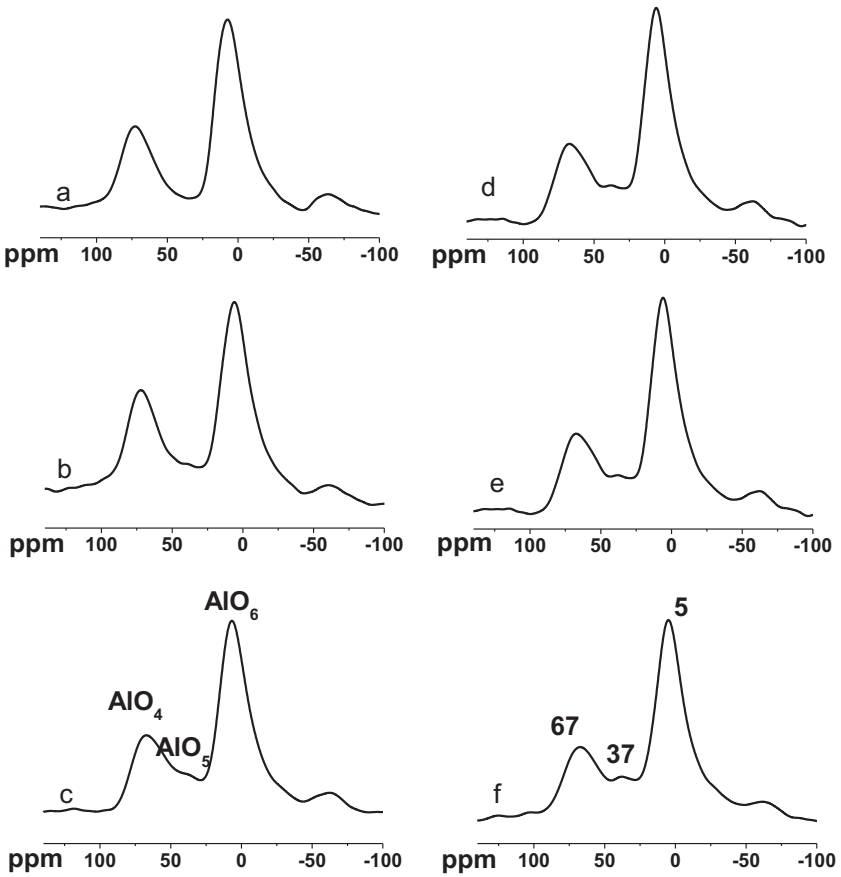

Fig. 3. ^{27}Al MAS NMR spectra of sulfated pristine alumina nanofibres and fibrous ZrO_2/Al_2O_3 nanocomposites obtained by calcination at 650 °C: (a) SA-F; (b) S–Zr-2; (c) S–Zr-5; (d) S–Zr-10; (e) S–Zr-15; (f) S–Zr-30.

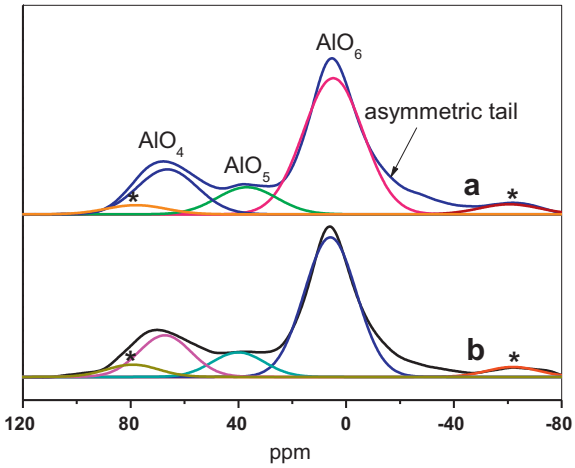

Fig. 4. Separated components of (a) S–Zr-30 and (b) S–Zr-50 obtained by spectrum fitting procedure. *Quadrupolar sideband.

at around 67 ppm indicates the presence of tetrahedral aluminium Al_{tetra} sites (AlO_4) [30]. These two resonances correspond to the two coordination states of Al in γ-Al_2O_3 crystal structure [31,32], which complements the XRD results of these nanocomposites. The alumina phase in S–Zr-50 could be confidently identified as γ-Al_2O_3. For all the samples, the resonance peaks corresponding to the AlO_6 are remarkably asymmetric, and a tail in spectra from 0 to −25 ppm can be observed. The tail could be due to the presence of new Al octahedral sites, namely $Al_{octa\text{-}O\text{–}S}$ or $Al_{octa\text{-}O\text{–}Zr}$, where S or Zr is located in the second coordination shell of aluminium [33]. In addition, with the increase in the Zr/Al molar ratio, a resonance between two main peaks centred at about 37 ppm becomes more pronounced. This component has been assigned to pentacoordinated aluminium Al_{penta} sites (AlO_5) [34].

It should be noted that in this work, γ-Al_2O_3 is prepared via the phase transformation of boehmite phase which only contains octahedral aluminium Al_{octa} sites (AlO_6). Both of AlO_4 and AlO_5 sites are created by the dehydration and dehydroxylaton of AlO_6 at elevated temperature. In Table 2 the relative percentages of the AlO_4, AlO_5 and AlO_6 are listed for the sample with increasing Zr molar percentages. It shows that the AlO_5 sites increase at the expense of both AlO_6 and AlO_4 sites, and the AlO_6 site decreased more rapidly than the AlO_4 site. The enhancement of AlO_5 sites with the increase in Zr molar percentages suggests that the penta-coordinated aluminium site is correlated to the surface interaction between zirconia and alumina. Nevertheless, the percentage of AlO_5 sites was not directly affected by the Zr content. For the sample S–Zr-10, the percentage of AlO_5 sites is slightly lower than that for the samples S–Zr-2 and S–Zr-5. Presumably, this is because at 10 mol% Zr, zirconia species transfer into tetragonal nanocrystallites and the Al–O–Zr sites are reduced due to the aggregation of zirconia species. Therefore, it is possible that when zirconia species is in highly dispersed state (S–Zr-2, S–Zr-5), the samples possess more AlO_5 sites.

Table 2
The relative percentages of the AlO_4, AlO_5 and AlO_6 species for the nanocomposites with various Zr molar percentages (obtained by spectrum simulation procedure).

Sample name	AlO_6	AlO_5	AlO_4
SA-F	74.8%	0%	25.2%
S–Zr-2	65.9%	6.7%	27.4%
S–Zr-5	66.1%	10.5%	23.4%
S–Zr-10	68.3%	7.6%	24.1%
S–Zr-15	67.1%	11.8%	21.2%
S–Zr-30	63.2%	13.8%	23.0%
S–Zr-50	62.1%	14.6%	23.3%

Table 3
The binding energies of Zr $3d_{5/2}$ photopeak corresponding to two kinds of Zr species and their relative ratios in XPS spectra.

Sample	Zr $3d_{5/2}$			
	ZrO_2	Percentage	Zr–O–Al	Percentate
S–Zr-50	182.9	100%	–[a]	–[a]
S–Zr-30	182.9	85%	183.8	15%
S–Zr-15	182.9	63%	183.8	37%
S–Zr-10	182.9	63%	183.8	37%
S–Zr-5	183.0	60%	183.8	40%
S–Zr-2	183.0	52%	183.8	48%

[a] Cannot be detected by XPS.

Particle morphology is investigated by SEM as shown in Fig. 5. The image for sulfated pristine alumina nanofibres shows many entangled worm-like particles. The fibrous morphology for this kind of material generates large inter-particle voids, which are referred to as porosity of this material. Importantly, after the sulfating procedure and calcination, the materials also retain their fibrous morphology which can be clearly observed from their SEM images. This structural stability is probably a result of the starting material, boehmite nanofibres, being relatively stable in sulfuric acid solution. This nanostructure is constituted by a singular or small bundle of nanofibres as a hard template and is further fixed by the zirconia shell. This zirconia shell is essential to maintain the integrity of the nanocomposite fibres. Therefore, short and thin nanofibres formed at low zirconia coverage and relatively large nanorods are observed when Zr percentage is higher than 15%. The porosity and pore volumes of these nanocomposites are dependent on the diameter and length of their constituted nanorods, which increase with the increase of Zr content, consequently, the macroporous frameworks resulting from specific morphology of fibrous nanomaterials are also gradually extended.

The transmission electron microscopy (TEM) images of S–Zr-30 and S–Zr-50 are illustrated in Fig. 6. Such solid acid nanocomposites exhibit a novel fibrous morphology where sulfated tetragonal zirconia shows irregular squares covering the alumina bundles. It can be observed that even at 30 mol% Zr content the sulfated tetragonal zirconia is still insufficient to cover the entire outer surface of alumina bundles while only at 50 mol% of Zr the bare alumina bundles are fully covered, indicating the outer surface of alumina bundles can bear an extremely large Zr content.

XPS analysis of pristine sulfated zirconia and all ZrO_2/Al_2O_3 nanocomposites was investigated and all samples were measured after crushing. Fig. 7a shows the Zr/Al XPS surface atomic ratios as a function of the corresponding overall ratios measured by EDX. When Zr molar percentage is equal to or less than 15%, the XPS ratios are very close to the bulk ratios. Above this value, the XPS surface ratios gradually become much higher than bulk ratio. Especially for the S–Zr-50, of which the bulk Zr/Al molar ratio is 1:1, the XPS surface ratio is close to 3:1, indicating the Zr species is concentrated on the outer surface of alumina nanobundles.

In addition, for S–Zr-50, the Zr $3d_{5/2}$ photopeak centred at binding energy of 182.9 eV (Fig. 7c), and only one chemical environment of Zr could be detected. This is the same with the result for pristine sulfated zirconia reported in the literature [35]. The interaction between the ZrO_2 species and Al_2O_3 support can only be detected when Zr molar percentage is lower than 30%, the Zr 3d photopeaks can be decomposed into two components (Fig. 7b). The binding energy of Zr $3d_{5/2}$ for one component is the same as pristine sulfated zirconia, and the other exhibits a displacement for the bonding energies of Zr $3d_{5/2}$ of 0.9 eV, to about 183.8 eV. This displacement has been associated with the formation of Zr–O–Al-type bonds [36]. The ratio of the latter component increases with decreasing of zirconium content, which is summarised in Table 3.

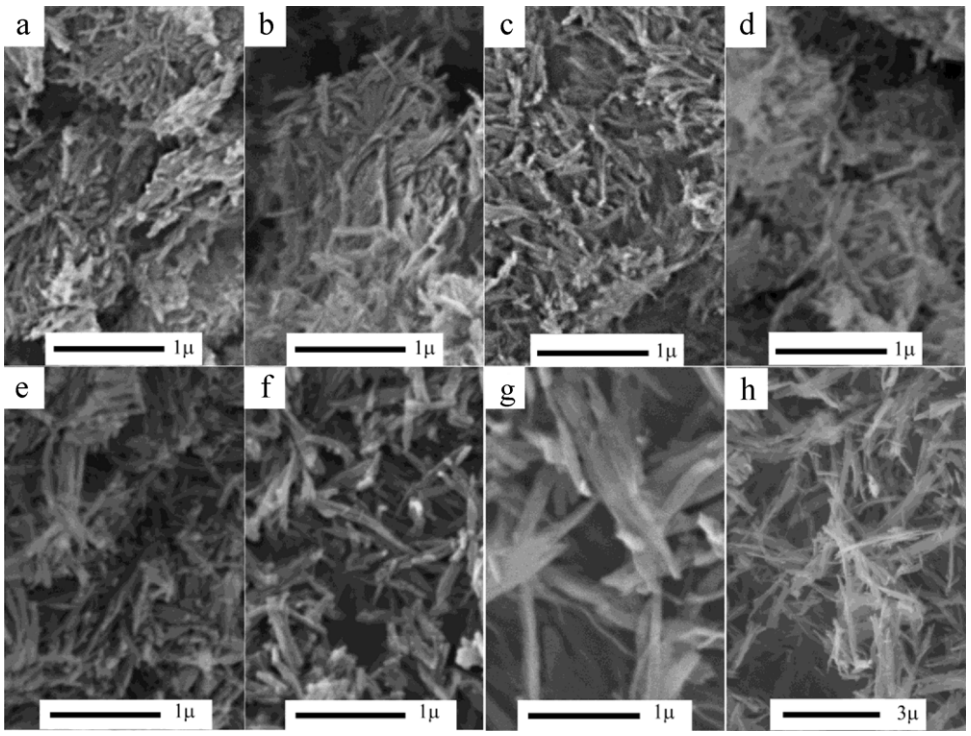

Fig. 5. SEM images of sulfated pristine alumina nanofibres and fibrous ZrO_2/Al_2O_3 nanocomposites obtained by calcination at 650 °C: (a) SA-F; (b) S–Zr-2; (c) S–Zr-5; (d) S–Zr-10; (e) S–Zr-15; (f) S–Zr-30; (g) S–Zr-50; (h) S–Zr-50 at a larger scale.

The BET surface areas and pore structures of these catalysts are determined by nitrogen adsorption–desorption isotherms. Fig. 8 shows those for representative samples to illustrate the textural changes with the increase of the Zr molar percentage. Accordingly, all the isotherms show a type IV characteristic feature of isotherm, which indicates that the samples examined are full of mesopores [37]. For S–Zr-50, the isotherms at high P/P_0 show a type II characteristic feature, which is often obtained in a macroporous material. The hysteresis of the three samples is quite different. The hysteresis loop of the sulfated alumina nanofibre falls within H3 and H4 categories, which, according to Sing's study [38], should be a result of slit-like pores constructed by plate-like particles. However this sample has the morphology of nanofibres. Therefore, the arrangement of nanofibres must also give rise to this kind of loop. The hysteresis for S–Zr-15 exhibits a loop with two steps: at high P/P_0 from 0.8 to 1.0, the hysteresis loop is close to H3, which show a higher slope ratio indicating wide slit-like pores; another step of hysteresis loops remains nearly horizontal over a wide range of P/P_0 from about 0.42–0.8, which is similar to the type H2 loop, associated with bottle ink pore or pore networks [39]. The former part is produced by the stacking of fibrous particles and the latter part is generated by the coating of zirconia nanocrystals and this is also observed for the sample S–Zr-50. For S–Zr-50, the adsorption branch and desorption branch overlapped at P/P_0 from 0.8–1.0, the isotherm become a combination of types II and IV adsorption, indicating the nanocomposite containing both mesopores and macropores [38].

The pore size distributions of as-synthesized nanocomposites (Fig. 9) are estimated from the adsorption branch of isotherm to avoid ambiguities arising from tensile strength effects [40]. Sample SA-F has a wide pore size distribution from 1 nm to 100 nm, which is the characteristic feature of pores arising from the intercrystallites voids constructed by nanofibres. All nanocomposites show two distributions from 1 to 8 nm and above 10 nm, respectively. The former

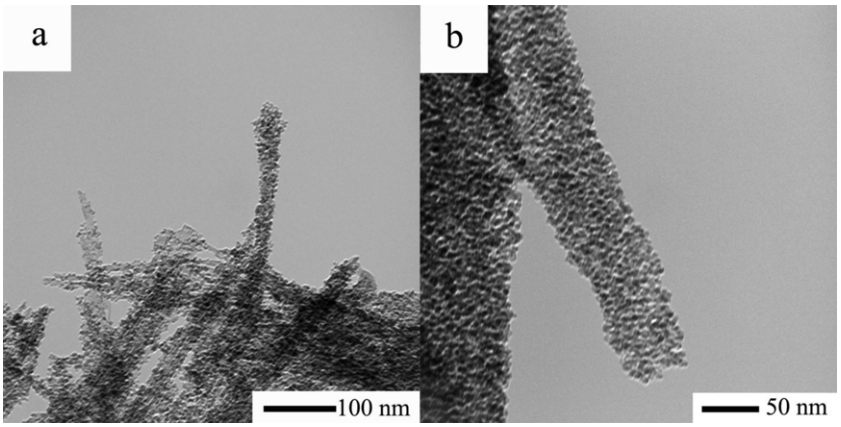

Fig. 6. TEM image for (a) S–Zr-30 and (b) S–Zr-50.

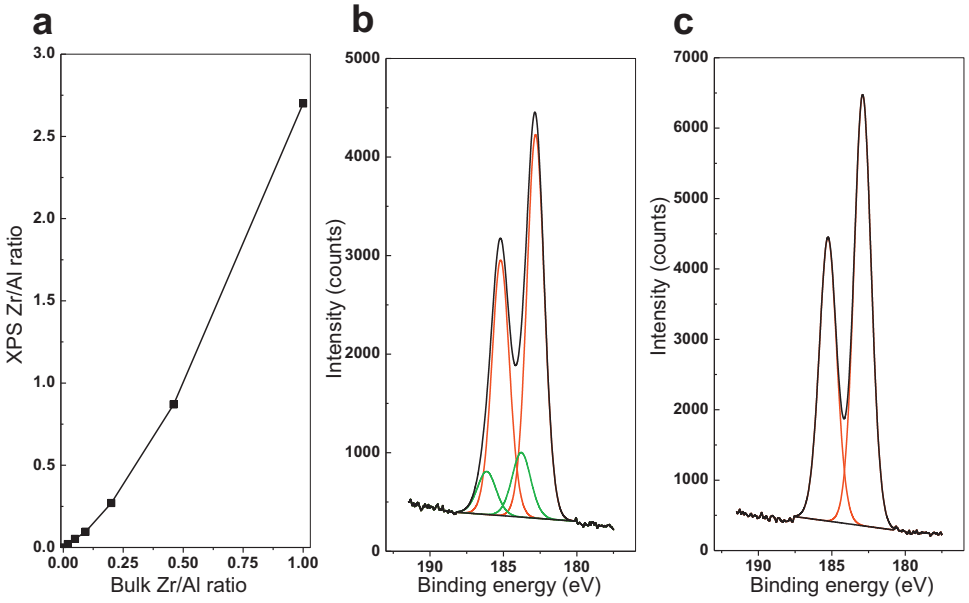

Fig. 7. XPS results (a) XPS Zr/Al molar ratio as a function of bulk Zr/Al molar ratio, (b) Zr 3d XPS spectra of S–Zr-30 and (c) Zr 3d XPS spectra of S–Zr-50.

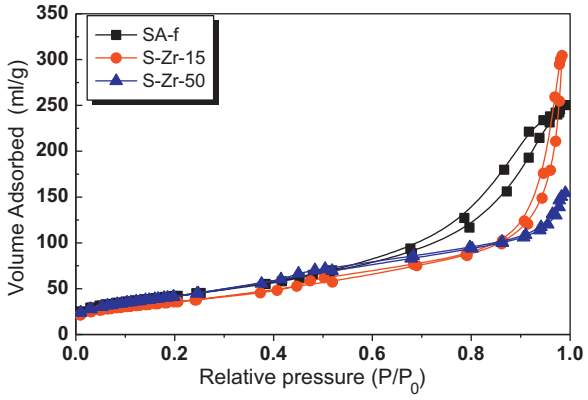

Fig. 8. Nitrogen adsorption and desorption isotherms for some representative samples with various Zr molar percentages.

distribution is attributed to the pores formed by incorporation of zirconia species and the latter one is assigned to those formed due to their fibrous morphology. It can be observed that the distribution from 1 to 8 nm gradually increases, while the latter distribution

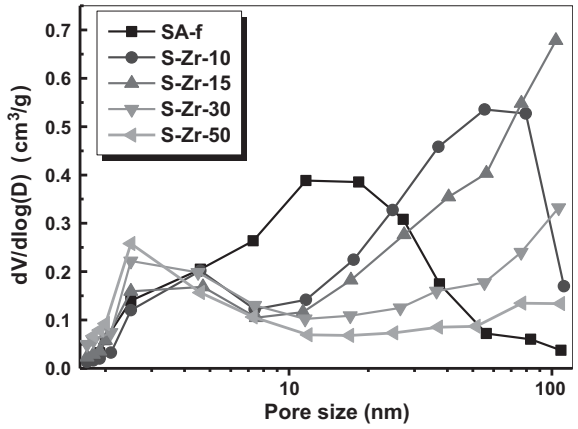

Fig. 9. Pore size distributions for samples with various Zr content.

decreases with the increase of Zr content. At 50 mol% Zr, pore size is mainly distributed in the range of 2–8 nm, the inter-particle voids resulting from fibrous nanostructure almost disappear. This phenomenon was also observed in our previous work [22] and is due to the increase of Zr mol% enhances the structural integrity (length and diameter increase) of resultant nanorods and the porous frameworks constructed from these fibrous nanocomposites gradually expand, leading to the most of macropores exceeding the measurable range for N_2 physisorption.

The main textural parameters for sulfated samples after calcination at 650 °C and original boehmite nanofibres are listed in Table 4. Many literatures confirm that loading even small amount of zirconia on alumina would result in a decrease in surface area, most prominently when zirconia crystal phase begins to appear, the surface area would dramatically be decreased below 100 $m^2\ g^{-1}$ [11,16,41]. However, interestingly in this work, samples with differing zirconia loading on alumina nanofibres actually maintain a relatively constant high specific surface area. The specific surface areas for all as-synthesized nanocomposites vary from 125 to 154 $m^2\ g^{-1}$. In contrast, the pristine sulfated zirconia has a surface area at about 88 $m^2\ g^{-1}$, similar to that reported in literature [20]. The sulfated alumina nanofibres exhibit a similar surface area, average pore size and pore volume comparing with original boehmite nanofibres.

The sulfated zirconia is an important solid acid catalyst. However, its acid strength is still in debate. At the very beginning,

Table 4
Powder properties of the sulfated fibrous ZrO_2/Al_2O_3 nanocomposites with various Zr molar percentage and sulfated alumina nanofibres obtained by calcination at 650 °C.

Sample	BET surface area ($m^2\ g^{-1}$)	Average pore size (nm)	Pore volume ($cm^3\ g^{-1}$)
Boehmite nanofibres	158	13.32	0.525
SA-F	152	10.16	0.387
S–Zr-2	138	16.42	0.565
S–Zr-5	131	16.47	0.540
S–Zr-10	125	15.74	0.491
S–Zr-15	128	14.67	0.471
S–Zr-30	154	8.26	0.318
S–Zr-50	153	6.25	0.239
SZ	88	7.69	0.169

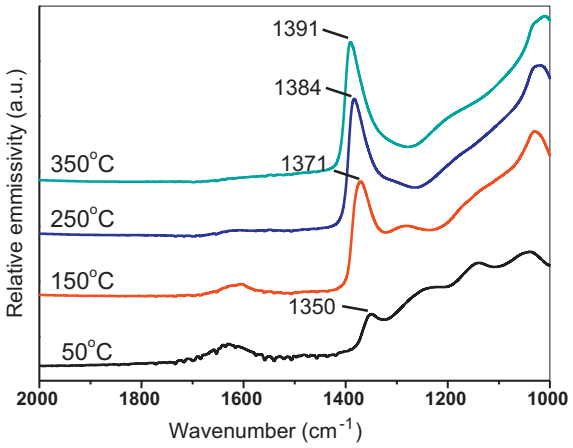

Fig. 10. Infrared emission spectra of S–Zr-50 in the region 2000–1000 cm^{-1} from 50 °C to 350 °C at 100 °C intervals.

sulfated zirconia was claimed to be a superacid which was defined as a material with acidity stronger than 100% H_2SO_4 [42]. The acid strength of sufated zirconia was measured by the change in color of a Hammett indicator at $pK_a \leq -14.52$, was estimated to be $H_0 \leq -16.04$. Based on this, the acidity was considered to be 10,000 times stronger than 100% perchloric or sulfuric acid [2]. However, when Umansky et al. [43] used the same Hammett indicator to measure the acidity of sulfated zirconia and recorded the color change by UV spectroscopy to minimize the experimental subjectivity, he reported that the acidity of sulfated zirconia was only equivalent to 100% H_2SO_4. Indeed, the use of Hammett indicators is also considered to be unreliable for the accurate measurement of solid acidity [44], because it was hard to achieve the equilibrium measurement using these indicators [45].

The superacidic protons of sulfated zirconia has been detected by ^{1}H NMR and Raman spectroscopic studies [46], and was considered to be significantly stronger than H-ZSM-5. Corma et al. [47] also reported the detection of superacid sites using temperature-programmed desorption of NH_3. However, the validity of some traditional techniques, such as temperature-programmed desorption [48,49] and IR study of pyridine adsorption [50] have been questioned for the determination of the acidity of sulfated zirconia, and was believed to inevitably misestimate the acidity of this kind of material. In contrast, numerous investigators have claimed that the acid strength of sulfated zirconia is similar to H-ZSM-5 and is only a strong acid, this was indicated by some advanced characterisation technologies, including ^{1}H, ^{13}C NMR spectroscopy [51], microcalorimetry [52–54], and infrared shifts of OH groups [55–57].

The measurement of acid strength of a solid acid is much more complex than determining that of a liquid acid. The solid acids are heterogeneous and the accessibility of acid sites makes the determination of acid strength of solid acids difficult [58]. Accurate evaluating of acid strength of solid acid is still challenging at this time [59,60]. Therefore, it is not surprising that different characterisation techniques will lead to discrepancies in results. Under these circumstances, the relative acid strength is measured in this work.

Fig. 10 shows the Fourier transform infrared emission spectroscopy (IES) of sulfated ZrO_2/Al_2O_3 nanocomposite (S–Zr-50) from 50 °C to 350 °C. According to the literature, the surface sulfur complexes formed by the interaction of metal oxides with sulfate ions, after evacuation at above 350 °C, exhibit a strong band at 1382–1391 cm^{-1} in mid-infrared spectroscopy which is assigned to S=O stretching vibration [17,61]. This band has a strong tendency to reduce its wavenumber with the adsorption of basic molecules such as H_2O. This wavenumber shift, corresponding to a decrease in the bond order of S=O covalent bond and an increase in the partial charge on oxygen atom [61], is associated with the acid strength of the catalyst, where larger wavenumber shifts correspond to higher acidity. Measuring the wavenumber shift of S=O by infrared spectra is regarded as a recommended method to detect the relative acid strength of the sulfated oxide catalysts [17,18].

Table 5
Effect of water adsorption on S=O including stretching frequency, bond order and partial charge on oxygen.

Sample	S=O wavenumber (cm^{-1})			Bond order		Partial charge on oxygen	
	B[a]	A[b]	Shift	B	A	B	A
SA-F	1378	1351	27	1.84	1.80	−0.16	−0.20
S–Zr-2	1380	1350	30	1.85	1.80	−0.15	−0.20
S–Zr-5	1382	1350	32	1.85	1.80	−0.15	−0.20
S–Zr-10	1384	1350	34	1.86	1.80	−0.14	−0.20
S–Zr-15	1387	1350	37	1.86	1.80	−0.14	−0.20
S–Zr-30	1389	1350	39	1.86	1.80	−0.14	−0.20
S–Zr-50	1391	1350	41	1.86	1.80	−0.14	−0.20
SZ	1391	1350	41	1.86	1.80	−0.14	−0.20
SZ[c]	1392	1352	40	1.87	1.80	−0.13	−0.20

[a] Before water adsorption; measured at 350 °C.
[b] After water adsorption; measured at 50 °C.
[c] Date from Gao's work in Ref. [18].

Moreover, IES can measure the vibration wavenumbers of the samples *in situ* at elevated temperature, which avoids the re-adsorption of water molecules on the surfaces of materials, just after dehydroxylation, due to exposure to air in either the quenching or infrared measurement step. As shown in Fig. 10, the IES of S–Zr-50 at 50 °C shows S=O bonds vibration centred at 1350 cm^{-1} and a broad band near 1630 cm^{-1} corresponding to the bending vibrations of the surface water and hydroxyl group, which can be observed at the same time. As the heating temperature increasing, the S=O bonds vibration become stronger and shift from 1350 at 50 °C to 1391 cm^{-1} at 350 °C, and at this temperature, the hydroxyl group bending vibrations almost disappeared. Notably, in this work, the band position corresponding to the stretching vibration of S=O bond of sulfated zirconia obtained at 350 °C agrees well with that of the same sample previously described in Gao's work [18] which was detected by infrared absorption spectroscopy at room temperature after evacuating at 350 °C, indicating that this S=O wavenumber shift is due to the dehydrolysis of samples rather than the change of measuring temperature.

Obviously, the spectra obtained at 50 °C represent the situation that the water is absorbed on the sulfated catalyst, and those obtained at 350 °C correspond to the samples previously evacuated at 350 °C. According to a literature [17], the relative acid strength of sulfated fibrous ZrO_2/Al_2O_3 nanocomposites with different Zr molar percentage can be determined by measuring the S=O shifts from 50 °C to 350 °C based on the IES results. The S=O stretching wavenumber, the bond order and partial charge on oxygen atom calculated according to formulations in the literature [61] for the series of sulfated ZrO_2/Al_2O_3 nanocomposites with different Zr molar percentage are presented in Table 5.

Although there is a slight deviation between this work and Gao's work due to the use of different experimental technology, it can be clearly observed that the S=O shifts of this series of samples increased with the increase of zirconia loading from 0 to 50%. On the other hand, when Zr content is 50%, the shift of S=O stretching is almost identical to that of the sulfated zirconia, indicating similar relative acid strength between S–Zr-50 and SZ. The relative acid strengths are in the order of SA-F < S–Zr-2 < S–Zr-5 < S–Zr-10 < S–Zr-15 < S–Zr-30 < S–Zr-50 ≈ SZ.

The sulfate contents in all samples are determined by ion chromatography (Table 6). Based on the surface area of each material, the densities of SO_4^{2-} groups could also be estimated, ranging from

Table 6
Surface area and sulfate content of various samples.

Samples	Surface area ($m^2\ g^{-1}$)	SO_4 content		
		wt%	$\mu mol\ g^{-1}$	groups/nm^2
SA-F	152	4.57%	452	1.8
S–Zr-2	138	4.34%	568	2.5
S–Zr-5	131	5.15%	536	2.5
S–Zr-10	125	6.70%	698	3.4
S–Zr-15	128	6.36%	663	3.1
S–Zr-30	154	5.86%	610	2.4
S–Zr-50	153	4.44%	463	1.8
SZ	88	2.52%	263	1.8

1.8 to 3.4 per nm^2. Given that the thermochemical radius of SO_4^{2-} is 2.30 Å [62], the value of the density of SO_4^{2-} groups may correspond to a monolayer dispersion of isolated SO_4^{2-}, assuming that the dispersion on the surface of all nanocomposites are homogeneous. However, the density of SO_4^{2-} groups for nanocomposite samples is obviously higher that of pristine sulfate samples (pristine ZrO_2 and Al_2O_3). In this work, it achieves maximum when Zr molar percentage is 10%. Therefore, it can be inferred that the interface of alumina and zirconia nanocrystallites could graft much more sulfate ion than a pristine metal oxide surface.

Benzoylation of toluene with benzoyl chloride is used to investigate the liquid acid-catalytic activity of as-synthesized fibrous solid catalysts. For all these sulfated nanocomposite catalysts, the products of the benzoylation reaction of toluene are a mixture of *p*-, *o*- and *m*-methylbenzophenone, respectively. The selectivity is not affected by the difference of acid strength, which is 67–69% of *p*-methylbenzophenone, 27–29% of *o*-methylbenzophenone, and 3–4% of *m*-methylbenzophenone in our experiments.

The catalytic activities of samples with different zirconia content are illustrated in Fig. 11. The temperature of reaction system is stabilised at reflux. From Fig. 11, it can be observed that when Zr content is up to 5%, the ketone yield is less than 25% for 6 h, but it is about 10% higher than that of the sulfated pristine alumina

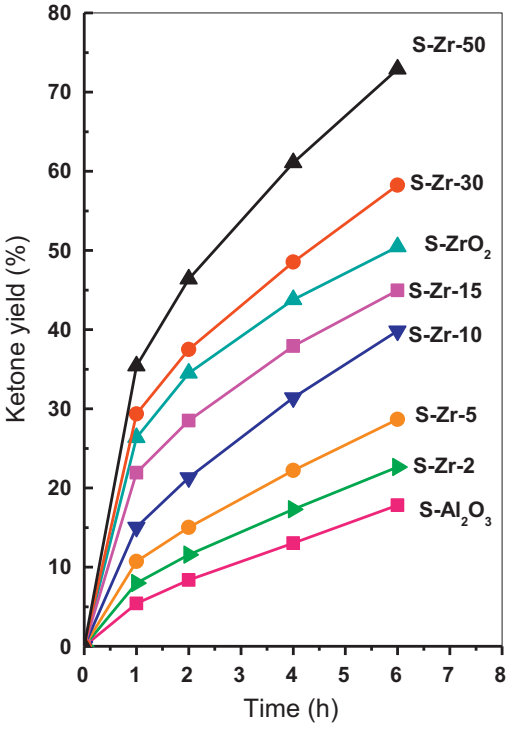

Fig. 11. Benzoylation of toluene at 110 °C.

nanofibres. As Zr content increases to 10%, the catalytic activity dramatically rises. The activity of the composite exceeds that of sulfated pristine zirconia at or above 30% Zr molar percentage. The overall tendency is that the catalytic activities increase with the increase in zirconia amount from 2% to 50%.

The ketone yield for H–Y is only 1.3% in 6 h, and it is only 2.6% for H-ZSM-5. However, the selectivity of products for zeolite catalysts are different from these sulfated nanocomposites catalysts. For zeolite HY, the selectivity for *p*-product is 78.3% and 21.6% for *o*-product. No *m*-product is observed because of the low productivity. For zeolite H-ZSM-5, the selectivity for *p*-product is 83.8%, 8.4% for *m*-product and 7.8% for *o*-product. Their different selectivity strongly indicates their differences in diffusivity. H-ZSM-5 possesses higher selectivity for *p*-methylbenzophenone attributed to its smaller pore size (5.5 × 5.9 Å) comparing with that of zeolite Y (7.4 Å) [63].

The relative acidities of sulfated catalysts are determined by IES in this work. It is believed that benzoylation reaction only proceeds on the very strong acid sites which are strong enough for the generation of the reaction intermediate, $PhCO^+$ cation [64]. Since the strong acid sites for all these nanocomposites catalyst are generated by the grafting of sulfate ions, their amount can be evaluated from their sulfate contents, which is obviously independent of the increase of catalytic activity. Combined with their relative acid strength of these catalysts, the catalytic performances of all nanocomposites exhibit that the stronger the relative acidity is, the higher the catalytic activity is. The catalytic activity dramatically rises at 10 Zr mol%. Taking the XRD results into account, tetragonal zirconia starts to form until the Zr mol% is above 10%, and with the increase of the Zr mol% the amount of tetragonal zirconia in the sample increases. This result, which coincides with the activities of samples, suggests the increase of tetragonal zirconia might relate with the enhancement of surface acidity of the catalyst.

The acid strength of H-ZSM-5 is stronger than that of HY, and its catalytic activity is also higher than that of HY in our experiment. Despite their poor catalytic activities, the correlation that stronger acid sites lead to higher catalytic activity is also complied by zeolite catalysts. It cannot be excluded that the low catalytic activities of H-ZSM-5 and HY in this reaction are possibly due to the lower accessibility of their acid sites in the narrow channels of zeolites. However, it should be mentioned that the solid acid possesses both Brønsted acid site (protonic sites) and Lewis acid sites (an electron-pair acceptor). The Brønsted acid strength of solid catalyst can be quantitatively measured by various characterisation techniques, while indeed an unambiguously measuring the strength of Lewis acids in a solid is impossible because their sequence may reverse against different probe molecules [65]. Despite of that, Lewis-type superacid sites present in sulfated zirconia was also suggested in literature [66–68], which may enhance the catalytic performance of vicinal protonic sites [58]. Moreover, the catalytic activity for model reaction of a solid acid should also be concerned as characterise its overall acid strength [58]. For sulfated nanocomposites and zeolite catalysts, the contradiction between their catalytic activities in this work and their reported similar acid strength clearly reveal some difficulties and uncertainties in measuring solid acid strength, indicating the necessity of an acceptable definition for solid superacid.

4. Discussion

Our previous work [22] has investigated the formation mechanism of fibrous ZrO_2/Al_2O_3 nanocomposites, and reveals that the tetragonal zirconia nanocrystallites evenly encompass the long bundle of boehmite nanofibres forming a core–shell structure. In this work the sulfation process only inflicts a negligible effect on the fibrous morphology of these nanocomposites with this

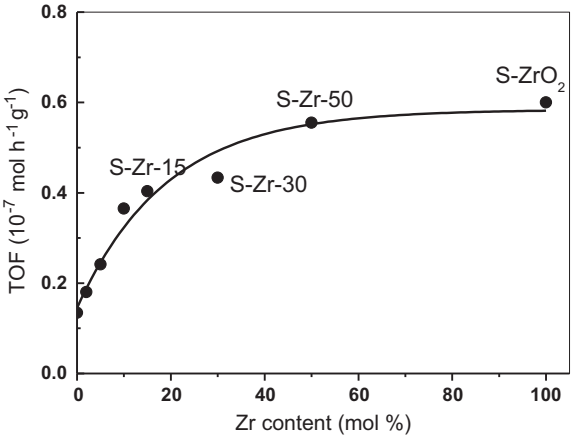

Fig. 12. Turnover frequencies of sulfated catalysts as a function of zirconia content.

effect also being minimized by the increase of zirconium coverage. Therefore, these zirconia nanocomposites with hierarchically macro–mesoporous nanostructures successfully develop into a novel class of solid strong acid.

An interesting result of these as-synthesized nanocomposite catalysts is that their specific surface areas remain constant with Zr molar percentage varying from 2% to 50%. This is quite different from the published data, in which it was reported that loading a heavy metal oxide on a porous carrier will result in the significant decrease of specific surface areas for resulting composites, especially, when the concentration of the loading species was high enough to generate some small independent nanocrystallites, where the surface areas would severely decrease under 100 m^2 g^{-1}. The reason of this phenomenon for traditional porous carrier is presumably that some of nanocrystallites block the orifices of porous materials [69].

In this work, the zirconium species are loaded on the long bundle of alumina nanofibres composing a fibrous core–shell structure with zirconium species concentrating on the outer-surface of these rod-like nanocomposites. At high Zr percentage, the growth and distribution of tetragonal zirconia nanocrystallites on fibrous cores at elevated temperature spontaneously form a mesoporous layer with pore size from 1 nm to 10 nm rather than plugging the orifices as been observed previously. These small zirconia nanocrystallites can provide a large specific surface area; therefore, in spite of the specific surface reduction caused by overlapping of the interface between zirconia nanocrystallites and alumina nanofibres, the overall surface areas of these nanocomposites will be not significantly decreased even at high loading ratio of heavy metal oxide. Indeed, it is confirmed by our experiments: at low Zr percentage, zirconia species are highly dispersed on the surface of γ-Al_2O_3 in a spontaneous process [70], and the surface area of nanocomposites slightly decreases due to the increase of apparent density, however, with the Zr percentage increasing to that high enough to generate zirconia nanocrystallites, new surface is also generated by the occurrence of tetragonal zirconia nanocrystallites leading to the increase of the surface areas. At this situation, the materials can bear extremely large loading ratios and their surface area and pore size seems to be independently modified. This can provide an effective approach to design a catalyst with a desired nanostructure, for instance, as observed in our previous work [22], the existence of interconnected macroporous framework increase the resistance to sintering of this materials at elevated temperature and minimize the aggregation of zirconia nanocrystallites, and should also efficiently transport guest molecules to the reactive sites. Therefore, the core–shell structure of nanocomposite catalysts and their fibrous morphology are emphasized to be important for catalytic application. As for this reaction, the catalytic performance is mainly determined by acid strength and surface area of as-synthesized nanocomposites with no evidence showed that the pore size and porous framework exerted any effect on the catalytic performance. Since all of nanocomposites catalysts possess similar surface areas, it is easy to conclude the relationship between the acid strength and catalytic activity is such that the pristine sulfated alumina nanofibres only contributes to lower activity; and that the increase in Zr concentration gradually increases the relative acid strength. Consequently, an increase in the catalytic activity of benzoylation of toluene was observed. It is worth mentioning that the acidity for the sample with 30% Zr molar percentage is slightly weaker than that of pristine sulfated zirconia, but compared with pristine sulfated zirconia, this sample possesses larger surface area which is 154 m^2 g^{-1}(reference catalyst is only 88 m^2 g^{-1}). The smaller tetragonal nanocrystals of about 3.9 nm attached on alumina nanofibres can generate more eligible active sites for this catalytic reaction. Above this Zr molar percentage, the nanocomposite exhibits higher catalytic activity because the enhancement of acid strength.

Moreover, the turnover frequencies of samples including pristine sulfated zirconia and fibrous sulfated nanocomposites are calculated based on their surface areas, and plotted as a function of zirconia contents (Fig. 12). The catalytic activity of per square meter for S–Zr-50 is very similar to sulfated pristine zirconia, even slightly lower than the pristine sample. As we mentioned above, the interface of alumina and zirconia nanocrystallites may accommodate much more sulfate ion than a pristine metal oxide surface, thereby generate much more acid site. However the increase of the amount of acid sites is independent of the increase of catalytic activity of these sulfated nanocomposite catalysts. This possibly due to the fact that even alumina is a promoter for the sulfated zirconia it mainly enhances the acid sites with intermediate acid strengths [18] rather than very strong acid sites needed by the reaction of benzoylation of toluene, while such acid sites has been observed to increase with increasing the amount of tetragonal zirconia. Since the pristine sulfated zirconia is slightly higher than S–Zr-50, the higher catalytic activity of core–shell nanocomposites is derived from the higher accessibility of acid sites of smaller tetragonal zirconia nanocrystallites rather than from higher acid strength.

5. Conclusions

A series of sulfated ZrO_2/Al_2O_3 nanocomposites with fibrous morphology were synthesized as new solid acid catalyst. The zirconium molar percentage was from 2% to 50%. Zr species is highly dispersed on alumina nanofibres at Zr molar percentage up to 5% and transferred into tetragonal zirconia nanocrystallites above 10%. Due to the core–shell structure, the surface Zr/Al molar ratios calculated from XPS results are higher than the bulk ratios when Zr molar percentage is above 15%, and which is about 3 times as much as bulk value at 50% of Zr molar percentage, suggesting an unambiguous core–shell structure formed. NMR results show that the interaction between zirconia species and alumina strongly correlates with pentacoordinated aluminium sites, which can also be detected by the dislocation of the bond energy 3d of the zirconium.

The relative acidity of the obtained fibrous sulfated core–shell nanocomposites increases with Zr molar percentage, but the samples maintain an almost constant, large specific surface area due to their unique nanostructure. Benzoylation of toluene is investigated using these novel strong solid acids. It is found that the catalytic activity of the catalyst is strongly related to the surface acidity of the catalyst. The amount of tetragonal zirconia and the resultant relative acidity of the catalyst increase with increasing Zr molar percentage. The sample with 50% of zirconium molar

percentage possesses the highest surface acidity equalled to the pristine sulfated zirconia as well as the highest catalytic performance. The catalytic activity of as-synthesized nanocomposites with 30% zirconium molar percentage surpasses that of the pristine sulfated zirconia due to the synergetic effect of the acid strength and enlargement of surface area.

Acknowledgements

The financial and infra-structure support from the Queensland University of Technology Chemistry Discipline is gratefully acknowledged. EML is thankful for a Queensland University of Technology doctoral scholarship. One author (WM) is grateful for the financial support in the form of an Australia Post-Doctoral Fellowship Provided by the Australian Research Council and a Smart State Fellowship provided by the Queensland State Government.

References

[1] V.C.F. Holm, G.C. Balley, Bartlesville, USA Patent 3,030,599 (1962).
[2] M. Hino, S. Kobayashi, K. Arata, J. Am. Chem. Soc. 101 (1979) 6439–6441.
[3] B.M. Reddy, M.K. Patil, Chem. Rev. 109 (2009) 2185–2208.
[4] A. Corma, Chem. Rev. 95 (1995) 559–614.
[5] M. Hino, K. Arata, Chem. Lett. (1979) 1259.
[6] M. Hino, K. Arata, J. Chem. Soc. Chem. Commun. (1979) 1148–1149.
[7] J.H. Clark, Acc. Chem. Res. 35 (2002) 791–797.
[8] G. Rothenberg, Catalysis: Concepts and Green Applications, Wiley-VCH Verlag GmbH & Co. KGaA, Weinheim, 2008.
[9] D. Farcasiu, J.Q. Li, Appl. Catal. A 175 (1998) 1–9.
[10] F.R. Chen, G. Coudurier, J.F. Joly, J.C. Vedrine, J. Catal. 143 (1993) 616–626.
[11] Y.-Y. Huang, B.-Y. Zhao, Y.-C. Xie, Appl. Catal. A: Gen. 173 (1998) 27–35.
[12] T. Jin, M. Machida, T. Yamaguchi, K. Tanabe, Inorg. Chem. 23 (1984) 4396–4398.
[13] C. Morterra, G. Cerrato, F. Pinna, M. Signoretto, J. Catal. 157 (1995) 109–123.
[14] G. Larsen, E. Lotero, R.D. Parra, L.M. Petkovic, H.S. Silva, S. Raghavan, Appl. Catal. A: Gen. 130 (1995) 213–226.
[15] B. Djuricic, S. Pickering, P. Glaude, D. Mcgarry, P. Tambuyser, J. Mater. Chem. 32 (1997) 589–601.
[16] J.R. Sohn, D.H. Seo, Catal. Today 87 (2003) 219–226.
[17] W. Hua, Y. Xia, Y. Yue, Z. Gao, J. Catal. 196 (2000) 104–114.
[18] Z. Gao, Y. Xia, W. Hua, C. Miao, Top. Catal. 6 (1998) 101–106.
[19] S.Y. Kim, N.J.G.G. Lohitharn Jr., R. Olindo, F. Pinna, P. Canton, Catal. Commun. 7 (2006) 209–213.
[20] P. Canton, R. Olindo, F. Pinna, G. Strukul, P. Riello, M. Meneghetti, G. Cerrato, C. Morterra, A. Benedetti, Chem. Mater. 13 (2001) 1634–1641.
[21] J. Zhao, Y. Yue, W. Hua, Z. Gao, Catal. Lett. 116 (2007) 27–37.
[22] E. Liu, Discipline of Chemistry, Queensland University of Technology, Brisbane, 2011.
[23] P. Laidlaw, D. Bethell, S.M. Brown, G.J. Hutchings, J. Mol. Catal. A 174 (2001) 187–191.
[24] A. Heidekum, M.A. Harmer, W.F. Hoelderich, J. Catal. 188 (1999) 230–232.
[25] G.D. Yadav, N.S. Asthana, V.S. Kamble, Appl. Catal. A: Gen. 240 (2003) 53–69.
[26] K. Arata, H. Nakamura, M. Shouji, Appl. Catal. A: Gen. 197 (2000) 213–219.
[27] S.C. Shen, W.K. Ng, Q. Chen, X.T. Zeng, M.Z. Chew, R.B.H. Tan, J. Nanosci. Nanotechnol. 7 (2007) 2726–2733.
[28] M. Hino, K. Arata, J. Chem. Soc. Chem. Commum. 1985 (1985) 112–113.
[29] J.T. Kloprogge, R.L. Frost, Phys. Chem. Chem. Phys. 1 (1999) 1641–1647.
[30] S. Moreau, M. Gervais, A. Douy, Solid State Ion. 101–103 (1997) 625–631.
[31] M.L. Guzman-Castillo, E. Lopez-Salinas, J.J. Fripiat, J. Sanchez-Valente, F. Hernandez-Beltran, A. Rodriguez-Hernandez, J. Navarrete-Bolanos, J. Catal. 220 (2003) 317–325.
[32] S.C. Shen, Q. Chen, P.S. Chow, G.H. Tan, X.T. Zeng, Z. Wang, R.B.H. Tan, J. Phys. Chem. C 111 (2007) 700–707.
[33] R. Iwamoto, C. Fernandez, J.P. Amoureux, J. Grimblot, J. Phys. Chem. B 102 (1998) 4342–4349.
[34] S.A. Bagshaw, T.J. Pinnavaia, Angew. Chem. Int. Ed. 35 (1996) 1102–1105.
[35] M.K. Younes, A. Ghorbel, J. Sol–Gel Sci. Technol. 26 (2003) 677–680.
[36] C.J. Dalmaschio, V.R. Mastelaro, P. Nascente, J. Bettini, J.L. Zotin, E. Longo, E.R. Leite, J. Colloid Interface Sci. 343 (2010) 256–262.
[37] S.J. Gregg, K.S.W. Sing, Adsorption, Surface Area and Porosity, Academic Press, London, 1982, pp. 111–190.
[38] K.S.W. Sing, D.H. Everett, R.A.W. Haul, L. Moscou, R.A. Pierotti, J. Rouquerol, T. Siemieniewska, Pure Appl. Chem. 57 (1985) 603–619.
[39] K.S.W. Sing, R.T. Williams, Adsorp. Sci. Technol. 22 (2004) 773–782.
[40] J.C. Groen, L.A.A. Peffer, J. Perez-Ramirez, Micropor. Mesopor. Mater. 60 (2003) 1–17.
[41] G. Li, W. Li, M. Zhang, K. Tao, Catal. Today 93–95 (2004) 595–601.
[42] R.J. Gillespie, Acc. Chem. Res. 1 (1968) 202–209.
[43] B. Umansky, J. Engelhardt, W.K. Hall, J. Catal. 127 (1991) 128–140.
[44] D. Farcasiu, A. Ghenciu, J.Q. Li, J. Catal. 158 (1996) 116–127.
[45] B.S. Umansky, W.K. Hall, J. Catal. 124 (1990) 97–108.
[46] T. Riemer, D. Spielbauer, M. Hunger, G.A.H. Mekhemer, H. Knozinger, J. Chem. Soc. Chem. Commum. 1994 (1994) 1181–1182.
[47] A. Corma, V. Fornes, M.I. Juan-Rajadell, J.M.L. Nieto, Appl. Catal. A: Gen. 116 (1994) 151–163.
[48] J.S. Lee, D.S. Park, J. Catal. 120 (1989) 46–54.
[49] E.C. Sikabwe, M.A. Coelho, D.E. Resasco, R.L. White, Catal. Lett. 34 (1995) 23–30.
[50] C. Morterra, G. Cerrato, Phys. Chem. Chem. Phys. 1 (1999) 2825–2831.
[51] H. Yu, H. Fang, H. Zhang, B. Li, F. Deng, Catal. Commun. 10 (2009) 920–924.
[52] G. Yaluris, R.B. Larson, J.M. Kobe, M.R. Gonzalez, K.B. Fogash, J.A. Dumesic, J. Catal. 158 (1996) 336–342.
[53] R.S. Drago, N. Kob, J. Phys. Chem. B 101 (1997) 3360–3364.
[54] J.C. Vartuli, J.G. Santiesteban, P. Traverso, N. Cardona-Martinez, C.D. Chang, S.A. Stevenson, J. Catal. 187 (1999) 131–138.
[55] V.J.W. Adeeva, D. Haan, J. Janchen, G.D. Lei, V. Schunemann, L.J.M.V.D. Ven, W.M.H. Sachtler, R.A.V. Santen, J. Catal. 151 (1995) 364–372.
[56] F. Babou, G. Coudurier, J.C. Vedrine, J. Catal. 152 (1995) 341–349.
[57] E.E. Platero, M.P. Mentruit, C.O. Arean, A. Zecchina, J. Catal. 162 (1996) 268–276.
[58] M.R. Guisnet, Acc. Chem. Res. 23 (1990) 392–398.
[59] J. Sommer, R. Jost, Pure Appl. Chem. 72 (2000) 2309–2318.
[60] N. Katada, T. Tsubaki, M. Niwa, Appl. Catal. A: Gen. 340 (2008) 76–86.
[61] T. Jin, T. Yamaguchi, K. Tanabe, J. Phys. Chem. 90 (1986) 4794–4796.
[62] G.D. Zhou, Inorganic and Structural Chemistry, Kexue Press, Beijing, 1982, p. 286.
[63] S.M. Auerbach, K.A. Carrado, P.K. Dutta, Handbook of Zeolite Science and Technology, Marcel Dekker, Inc., New York, 2003.
[64] Y. Xia, W. Hua, Z. Gao, Catal. Lett. 55 (1998) 101–104.
[65] G.A. Olah, G.K.S. Prakash, A. Molnar, J. Sommer, Superacid Chemistry, John Wiley & Sons, Inc., Hoboken, New Jersey, 2009.
[66] N. Katada, J.-I. Endo, K.-I. Notsu, N. Yasunobu, N. Naito, M. Niwa, J. Phys. Chem. B 104 (2000) 10321–10328.
[67] F.R. Chen, G. Coudurier, J.-F. Joly, J. Vedrine, J. Catal. 143 (1993) 616–626.
[68] C. Morterra, G. Cerrato, F. Pinna, M. Signoretto, G. Strukul, J. Catal. 149 (1994) 181–188.
[69] H. Rotter, M.V. Landau, M. Carrera, D. Goldfarb, M. Herskowitz, Appl. Catal. B: Environ. 47 (2004) 111–126.
[70] Y.-C. Xie, Y.-Q. Tang, Advances in Catalysis, Academic Press, New York, 1990.